PERGAMON

International Journal of Heat and Mass Transfer 43 (2000) 1243–1259

International Journal of HEAT and MASS TRANSFER

www.elsevier.com/locate/ijhmt

Large eddy simulation with a dynamic subgrid-scale model of turbulent heat transfer in an orthogonally rotating rectangular duct with transverse rib turbulators

Akira Murata[a,*], Sadanari Mochizuki[b]

[a]*Graduate School of Bio-Applications and Systems Engineering, Tokyo University of Agriculture and Technology, 2-24-16 Nakacho, Koganei, Tokyo 184-8588, Japan*

[b]*Department of Mechanical Systems Engineering, College of Engineering, Tokyo University of Agriculture and Technology, 2-24-16 Nakacho, Koganei, Tokyo 184-8588, Japan*

Received 21 July 1998; received in revised form 10 April 1999

Abstract

In order to investigate the effects of transverse ribs, the Coriolis force, and cross-sectional aspect ratios on turbulence, the large eddy simulation was performed changing the rotation number and the aspect ratio. The results reproduced the experimentally observed high heat transfer areas: in front of the rib on the rib-roughened walls and around the rib on the smooth side walls. In the rotating case, an interesting dissimilarity between the velocity and temperature fields was seen. The heat transfer enhancement caused by the rotation was larger for the higher aspect ratios because of the intensified Coriolis induced secondary flow.

Keywords: Heat transfer; Heat transfer enhancement; Turbulent flow; Finite difference method; Gas turbine; Blade cooling; Large eddy simulation; Coriolis force; Rib turbulator

1. Introduction

In the development of high performance gas turbines, effective blade cooling is essential because the higher efficiency of the turbine requires a higher inlet gas temperature. Generally, this blade cooling is performed by film cooling at the external surface of the turbine blade and also by internal forced-convection cooling which uses winding flow passages inside the turbine blade. In internal forced-convection cooling, the real phenomena are very complicated due to external forces: the Coriolis force and the buoyancy force in the centrifugal acceleration field. In addition to these external forces, the effects induced by a 180° sharp turn and turbulence promoters (ribs) installed on the internal surface result in phenomena that are beyond understanding [1].

Many researchers have investigated internal forced-convective cooling experimentally [2]. As for the local heat transfer of a rib-roughened duct, several researchers investigated the spatial variation of the local heat transfer with various techniques: wall temperature measurement by using hundreds of thermocouples [3–5], naphthalene sublimation technique to measure the local mass transfer, which was transformed into heat transfer by using the analogy between heat and mass

* Corresponding author. Tel.: +81-42-388-7089; fax: +81-42-385-7204.

E-mail address: murata@mmlab.mech.tuat.ac.jp (A. Murata).

0017-9310/00/$ - see front matter
PII: S0017-9310(99)00205-7

Nomenclature

A_R	duct cross-sectional aspect ratio ($= H/W$)
c_p	specific heat
C_f	friction coefficient ($= \tau_w/(0.5\rho U_m^2)$)
C_S	Smagorinsky constant
D	hydraulic diameter ($= 2HW/(H+W)$)
F_i	external force term
h	heat transfer coefficient
H	duct height
j	Colburn's j factor ($= Nu_m/(Re_m Pr^{1/3})$)
ℓ	length scale ($=0.5D$)
L_p	peripheral location
Nu	Nusselt number ($= hD/\lambda$)
Pr	Prandtl number ($=0.71$)
Pr_{SGS}	Prandtl number of subgrid-scale model ($=0.5$)
$\dot{q}$	wall heat flux
Re_m	Reynolds number ($= U_m D/\nu$)
Re_*	turbulent Reynolds number ($= u_*\ell/\nu$)
Ro_m	rotation number ($= \omega D/U_m$)
Ro_*	rotation number ($= \omega\ell/u_*$)
S_{ij}	rate-of-strain tensor
t	time
T	temperature
T_b	bulk temperature
T_r	friction temperature ($= \dot{q}/(\rho c_p u_*)$)
u, v, w	velocities in x, y, z directions
u_*	friction velocity
U_m	mean velocity
W	duct width
x, y, z	transverse, vertical, streamwise directions
Δx, Δy, Δz	grid spacing in x, y, z directions
α_{SGS_j}	subgrid-scale energy flux
λ	thermal conductivity
ν	kinematic viscosity
ν_t	subgrid-scale eddy viscosity
ω	angular velocity
ρ	density
θ	dimensionless temperature ($= (T - T_b)/T_r$)
$\tau_{SGS_{ij}}$	subgrid-scale stress tensor
τ_w	wall shear stress

Subscripts/superscripts

b	bulk
B	Blasius
L	local value
m	duct average or based on mean velocity
w	wall
∞	fully developed
*	friction velocity
+	dimensionless value based on inner scales

transfer [6,7], and wall temperature measurement by using temperature-sensitive liquid crystal [8,9]. In these studies, the heat transfer variation induced by the flow separation and reattachment behind the rib was captured to a certain extent. However, it is difficult to perform experiments in a rotating condition which can identify the flow structure and its influence on the heat transfer. Thus, further progress in experimental studies has been prevented so far.

In previous numerical studies, most researchers adopted the Reynolds average Navier–Stokes equation with a turbulence model. Although the approach that uses the Reynolds average turbulence model could reproduce the heat transfer of blade cooling to a certain extent for a rotating smooth duct [10], the turbulence model itself includes empirical constants and functions which have to be adjusted depending on the flow field. Launder et al. [11] pointed out that in order to quantitatively simulate the flow in a rotating system, the second moment closure, that is, the Reynolds stress equation model, is a minimum requirement considering a non-isotropic effect of the Coriolis force on turbulence. Recent advancement in computers enables us to numerically simulate the fluctuating components of the turbulent flow by using the large eddy simulation (LES) or the direct numerical simulation (DNS). Because LES and DNS directly resolve temporal variation of the fluctuating components, the results are more universal, in other words, more free from the empirical modeling than the Reynolds average turbulence models. So far, the turbulent flow in a stationary smooth duct with a square cross section was solved using DNS [12,13] and LES [14,15]. As for the rib-roughened case, only a numerical study by using the k–ε two equation turbulence model is reported [16]. For the flow with separation and reattachment, there emerges a problem in a damping factor which reproduces the wall proximity effect in a turbulence model, because the damping factor contains a dimensionless distance from the wall, y^+, which is not definable for such a flow in which a friction velocity locally becomes zero. The same problem also appears even when LES is applied, as far as the Smagorinsky model is used as a subgrid-scale (SGS) model. Therefore, a dynamic SGS model must be used instead for complicated flow cases [17].

The authors' group has performed heat transfer measurements by using thermocouples in both stationary and rotating conditions [3–5]. Very recently, numerical analyses were also performed by using the dynamic SGS model for a rotating smooth duct of which cross section was square [18] and rectangular [19], and the technique was further applied to a rotating rib-roughened square duct [20]. For the rib-roughened duct case, however, the numerical result could not give satisfactory symmetry because of the small sample size limited by the high computational load and the small number of homogeneous directions of the phenomena [20]. Moreover, considering that the cross section of the cooling flow passage for a real gas turbine is not square but rectangular (transversely narrow), the effect of the duct aspect ratio should be investigated.

This study deals with a fully developed turbulent flow and heat transfer in a rib-roughened rectangular duct by using the large eddy simulation. As for the subgrid-scale model, the dynamic subgrid-scale model was adopted considering the highly three-dimensional flow structure of the rib-roughened duct. The effects of the flow separation and reattachment caused by the ribs, the Coriolis force, and the duct cross-sectional aspect ratio on the heat transfer are examined, and the relation between the heat transfer enhancement and the flow structure is discussed.

2. Numerical analysis

Fig. 1 shows the computational domain and coordinate system used in this study. The duct had a rectangular cross section with a duct height of H and a duct width of W. The hydraulic diameter, D, was calculated as $2HW/(H+W)$. The coordinate system was fixed to a rotating duct which had an angular velocity of ω. The streamwise (radially outward) direction was chosen in the z direction; the x and y directions were transverse and perpendicular directions to trailing and leading walls, respectively. In this study, the duct cross-sectional aspect ratio, A_R $(=H/W)$, was varied among 1.0, 2.0, and 4.0 maintaining the same hydraulic diameter. Ribs were transversely installed on trailing and leading walls. The cross section of the rib was square (side length of $0.1D$) and streamwise pitch was set equal to the hydraulic diameter, D. This rib arrangement gave the rib height-to-hydraulic diameter ratio of 0.1 and the rib pitch-to-rib height ratio of 10, and it was the same as that in the experimental study of Ref. [5]. This rib arrangement was chosen because it was within the previously reported optimal range [21,22].

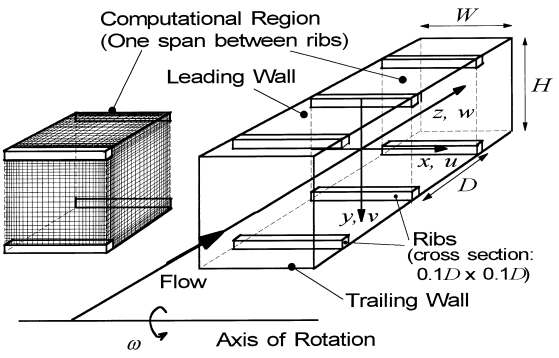

Fig. 1. Schematic of a rotating rib-roughened duct and coordinate system.

The procedure of the numerical analysis is the same as our previous studies [18–20]; thus, the procedure will briefly be explained. After applying a filtering operation to the incompressible Navier–Stokes equation with a filter width equal to the grid spacing [14], the dimensionless governing equations scaled by a length scale, ℓ $(=0.5D)$, and mean friction velocity, u_*, become a set of dimensionless governing equations with respect to grid resolvable components indicated by overbars as $(\bar{u}, \bar{v}, \bar{w})$ under the assumption of constant fluid properties. In order to simulate a fully developed situation, the pressure and temperature fields were decomposed into the steady and streamwisely linear component and the remaining component [23]. By this decomposition, the pressure and temperature fields became homogeneous in the streamwise direction. As shown in Eq. (1), F_i is an external force term including the Coriolis force, and the buoyancy term was ignored in this study. The mean pressure gradient term (with a value of 2) was added to the external force term as shown in Eq. (1).

$$F_i = \begin{pmatrix} 0 \\ 2Ro_*\bar{w} \\ -2Ro_*\bar{v}+2 \end{pmatrix}. \tag{1}$$

Because the mean pressure gradient which drove the flow in the streamwise direction was set to be constant in this study, the flow rate varied depending on the flow conditions (aspect ratios and rotation number); therefore, the flow rate was not known a priori, and the flow rate was calculated from the resultant computed flow field after the fully developed condition was attained.

The temperature was made dimensionless by using a bulk temperature, T_b, and a friction temperature, T_r, as $\theta=(T-T_b)/T_r$. Accordingly, the dimensionless energy equation was derived for the grid resolvable component, $\bar{\theta}$.

Subgrid-scale components of stress, $\tau_{SGS_{ij}}$, and energy flux, α_{SGS_j}, are expressed as follows:

$$\tau_{\mathrm{SGS}_{ij}} = 2\nu_{\mathrm{t}}\bar{S}_{ij} \quad \text{and} \quad \alpha_{\mathrm{SGS}_j} = \frac{\nu_{\mathrm{t}}}{Pr_{\mathrm{SGS}}}\frac{\partial\bar{\theta}}{\partial x_j}, \tag{2}$$

where

$$\bar{S}_{ij} = \frac{1}{2}\left(\frac{\partial\bar{u}_i}{\partial x_j} + \frac{\partial\bar{u}_j}{\partial x_i}\right), \tag{3}$$

$$\nu_{\mathrm{t}} = C_{\mathrm{S}}^2(\Delta x\Delta y\Delta z)^{2/3}\sqrt{2\bar{S}_{ij}\bar{S}_{ij}}. \tag{4}$$

In this study, the dynamic subgrid-scale model developed by Germano et al. [24] was used in order to calculate the value of C_{S} as a function of spatial location with the stable computational procedure of Lilly [25]. The turbulent Prandtl number for the subgrid-scale component, Pr_{SGS}, was set to 0.5 [26]. The width of the test filter was double the grid spacing and the space filter was accurate to fourth order [17].

The local Nusselt number, Nu_{L}, was calculated from the wall temperature as follows:

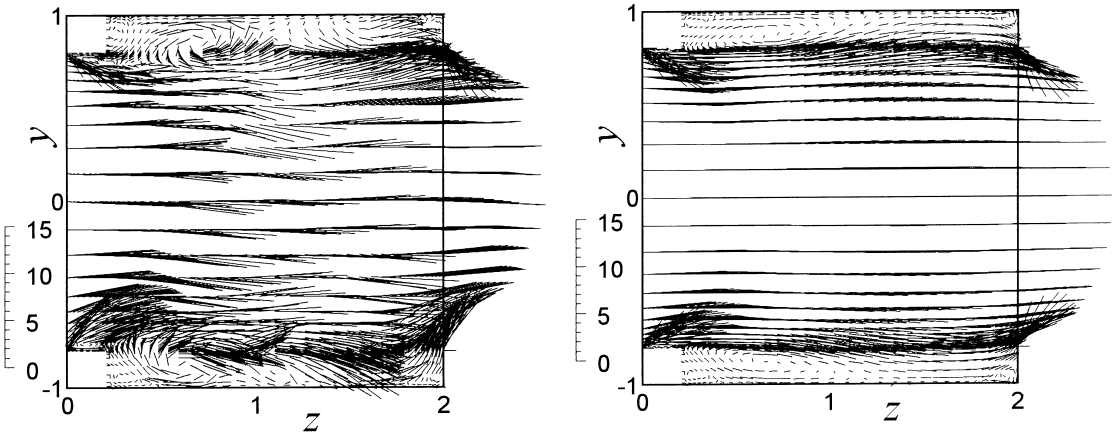

(a) Ro_*=0

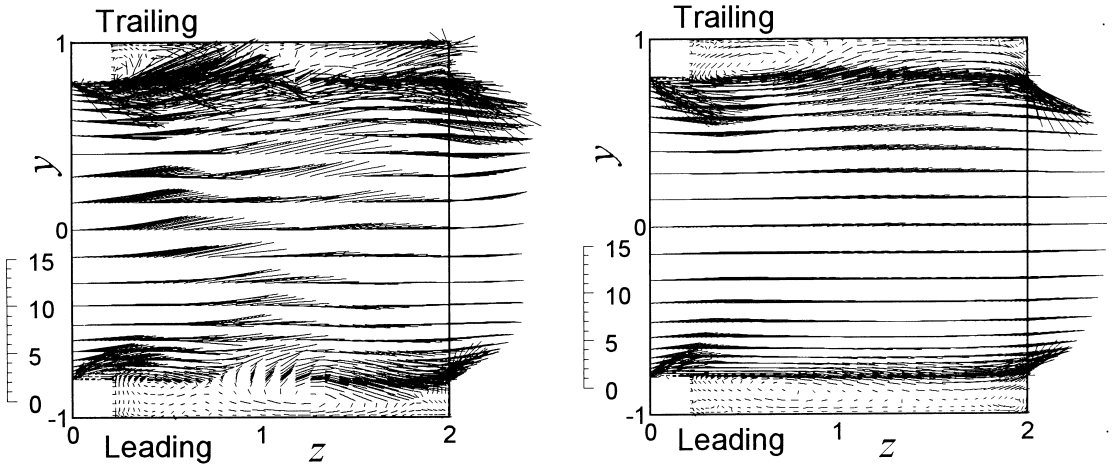

(b) Ro_*=1.0

Fig. 2. Velocity vectors in y–z plane at transverse center ($x = 0$). (Left and right figures are for instantaneous and time-averaged vectors, respectively. The scale on the left hand side of each figure indicates the vector magnitude.)

$$Nu_L = \frac{2Re_* Pr}{\bar{\theta}_w - \bar{\theta}_b}. \quad (5)$$

The inclusion of the dimensionless bulk temperature, $\bar{\theta}_b$, in Eq. (5) may seem unnecessary judging from the definition of the dimensionless temperature. However, the inclusion was necessary because the use of the periodic boundary condition did not allow $\bar{\theta}_b$ to be imposed to zero. The averaged Nusselt number was calculated by using the integrally averaged temperature difference for the area in question.

The bulk temperature was defined using the absolute value of the streamwise velocity as follows:

$$\bar{\theta}_b = \frac{\int\int \bar{\theta}|\bar{w}|\,dx\,dy}{\int\int |\bar{w}|\,dx\,dy} \quad (6)$$

This definition is one of the possible choices for the bulk temperature; however, even when the raw value, $\bar{w}$, was used instead of $|\bar{w}|$ in Eq. (6), the difference in the resultant $\bar{\theta}_b$ was less than 3% within the present computational conditions.

Discretization was performed by a finite difference method. The spatial and temporal discretization schemes were similar to those of [13]: the second-order central differencing method and the Crank–Nicolson method for the viscous term and the second-order differencing method satisfying the conservative property [27] and the second-order Adams–Bashforth method for the convective term. The external force term was also treated by the second-order Adams–Bashforth method. The pressure field was treated following the SMAC method [28], and the algebraic equation for each variable was solved by using the SOR method. The computational domain was one span between streamwise consecutive ribs (see Fig. 1) and its dimension was $2 \times 2 \times 2$, $1.5 \times 3 \times 2$, and $1.25 \times 5 \times 2$ in x, y, z directions for $A_R = 1.0$, 2.0, and 4.0, respectively. This can be expressed by using an inner length scale, v/u_*, as $700 \times 700 \times 700$ for the stationary case of $A_R = 1.0$.

The turbulent Reynolds number, Re_* $(= u_*\ell/v)$, was 350, and the rotation number, Ro_* $(= \omega\ell/u_*)$, was 0 and 1.0. In addition to these two cases of the rotation number, in order to see the effect of the rotation number, the computation with reduced total time steps (one-tenth of the large sample size for $Ro_* = 0$ and 1.0) was also performed varying Ro_* from 0 to 5.0. The Reynolds number, Re_m, defined by the mean velocity and the hydraulic diameter was about 4100, 5800, and 9200 for $A_R = 1.0$, 2.0, and 4.0, respectively, for the stationary case. As explained before, the value of Re_m was calculated from the result of computation; Re_m was not known a priori. At the wall boundary, no-slip and constant heat flux conditions were imposed, although the rib side surfaces were set to be adiabatic. At the inlet and outlet boundaries, the periodic boundary condition [23] was imposed in order to obtain a fully developed flow.

Staggered grids in the physical domain were contracted to both the walls and the rib surfaces by using a tangent hyperbolic function (see Fig. 1). This physical domain was transformed into a computational domain of uniform grid spacing. The grid number was $47 \times 47 \times 47$, and this grid configuration gave a grid spacing of $\Delta x^+ = 1.0$–38, $\Delta y^+ = 0.6$–52, and $\Delta z^+ = 3.6$–28 for the stationary case of $A_R = 1.0$. The effect of the grid spacing on the computed result was checked by increasing the grid number to $65 \times 65 \times 65$ for several cases, and no major difference was observed. Because the boundary condition was prescribed on the rib surface, the temperature field inside the rib was not solved. The time step interval was $\Delta t = 1.0 \times 10^{-4}$, which can be expressed as $\Delta t^+ = 0.035$ when made dimensionless by an inner time scale, v/u_*^2. The computation was started using the lower rotation number result as an initial condition. The calculations were carried out to 120,000 steps to fully develop the flow. After the initial 120,000 steps were performed, an additional 400,000 steps ($t = 40$ or $t^+ = 14{,}000$) were performed for computing the statistical values. This 400,000 step computation needed about 206,000 CPU seconds using an NEC SX4B. In our previous study [20], the fourth order scheme for the spatial discretization was used in contrast to the second order scheme adopted here. In this study, the lower order scheme was used because of its lighter computational load in order to obtain sufficiently symmetric results by increasing the total time step to be ten times larger than that in the previous study [20].

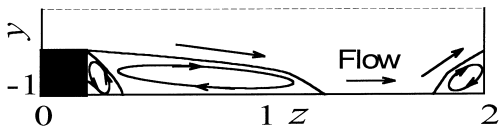

(a) Ro_*=0

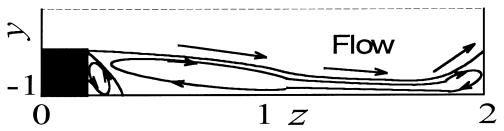

(b) Leading side for Ro_*=1.0

Fig. 3. Sketch of time-averaged flow pattern drawn from Fig. 2 near rib-roughened wall in y–z plane at transverse center ($x = 0$).

The influence of this scheme change will be discussed in detail later in Section 3.3.

3. Results and discussion

3.1. Square duct case (aspect ratio, $A_R = 1.0$)

Fig. 2 shows the velocity vectors in the y–z plane at the transverse center ($x = 0$). In the figure, left and right figures show instantaneous and time-averaged vectors, respectively. In Fig. 3, the sketch of the near-wall flow pattern drawn from Fig. 2 is shown for easier understanding. In the stationary case of Fig. 2(a), the time-averaged vectors show symmetry with respect to the horizontal plane of $y = 0$. It is clearly seen that the flow behind the rib separates and then reattaches at about the mid-point between the streamwise consecutive ribs. In Fig. 2(b), the effect of rotation is seen in the higher intensity of the flow passing beyond the upper rib on the trailing wall. This flow behavior is explained by Coriolis induced secondary flow which transports the fluid momentum from the leading side to the trailing side at the transverse center.

Fig. 4 shows the time-averaged velocity vectors in the x–y plane at rib location ($z = 0.1$; left figures) and between the consecutive ribs ($z = 1.1$; right figures) for the stationary (a) and rotating (b) cases. Here again,

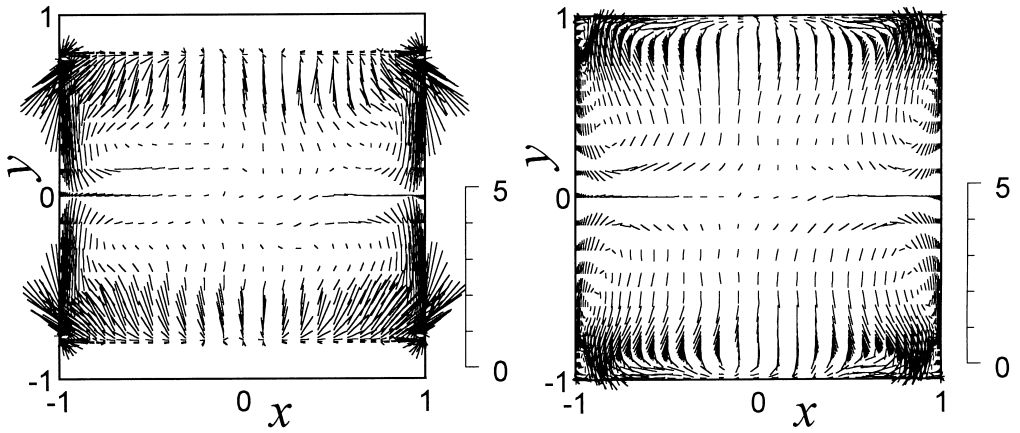

(a)Ro_*=0

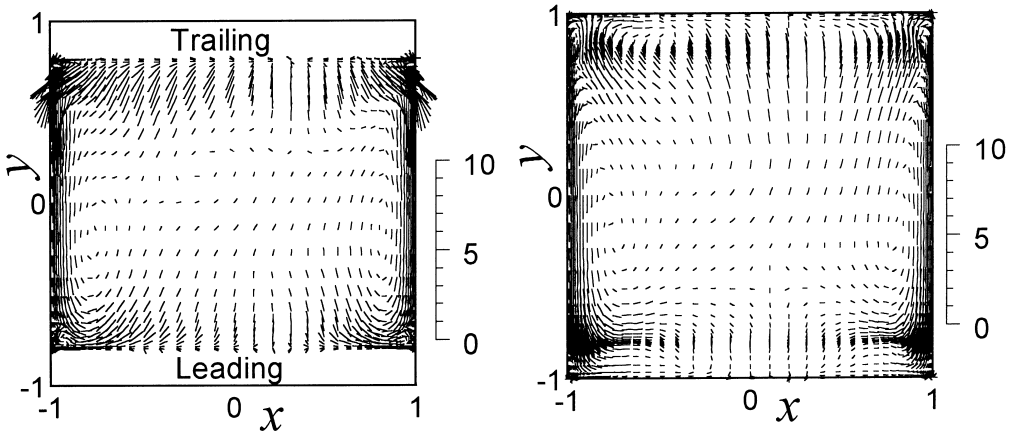

(b) Ro_*=1.0

Fig. 4. Time-averaged velocity vectors in x–y plane (aspect ratio, $A_R = 1.0$; left and right figures are at the streamwise locations above rib and between ribs, respectively. The scale on the right hand side of each figure indicates the vector magnitude).

the sketch of the flow pattern drawn from Fig. 4 is shown in Fig. 5 for easier understanding. Above the rib, the vertical velocity component leaving from the rib is clearly seen in Fig. 4(a) (left). Near the smooth side walls, the existence of the rib induces the flow going from the rib side to the horizontal symmetric plane ($y = 0$) as previously observed in the experiments [8,29]. In the plane between the ribs of Fig. 4(a) (right), the flow directing to the rib-roughened (upper and lower) walls is seen near these walls. This flow can be understood by considering the reattachment of the separated flow occurring at around the mid-point between the ribs. This flow then changes its direction to the side walls, although the flow directing to the opposite direction (to the center) is seen in the region very close to the rib-roughened wall. Near the smooth side walls of Fig. 4(a) (right), the flow directing to the horizontal symmetric plane similar to that in the plane above the rib of Fig. 4(a) (left) still prevails. When the duct rotates, in the plane above the rib of Fig. 4(b) (left), the flow seems intensified on the trailing side ($y = 1$) and suppressed on the leading side ($y = -1$). The flow structure near the smooth side walls is changed from the stationary case by the secondary flow induced by the Coriolis force, and the secondary flow sweeps the smooth side wall from the top (pressure side) to the bottom (suction side). In the plane between the ribs (Fig. 4(b) (right)), the flow structure near the trailing wall is similar to that of the stationary case, although near the leading wall the Coriolis induced secondary flow dominates.

Fig. 6 shows the isocontours of the time-averaged streamwise velocity, $\bar{w}$, and temperature, $\bar{\theta}$, in the x–y planes at the same streamwise location as Fig. 4. Similar profiles between $\bar{w}$ and $\bar{\theta}$ are obtained in the plane of the rib location (Fig. 6(a) and (c)). On the other hand, the velocity boundary layer of the upper and lower walls is much thicker than that of the ther-

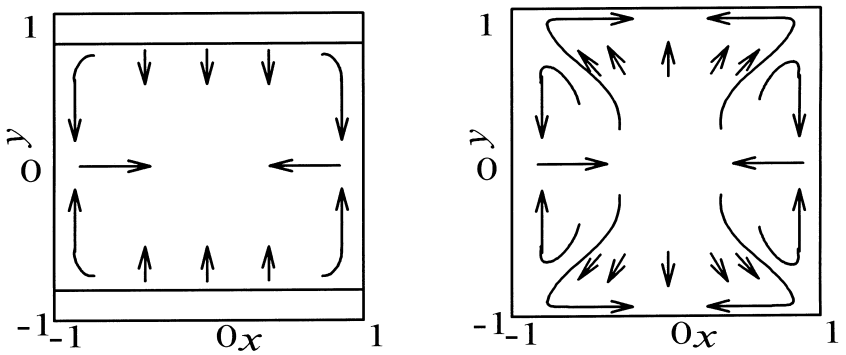

(a)Ro_*=0

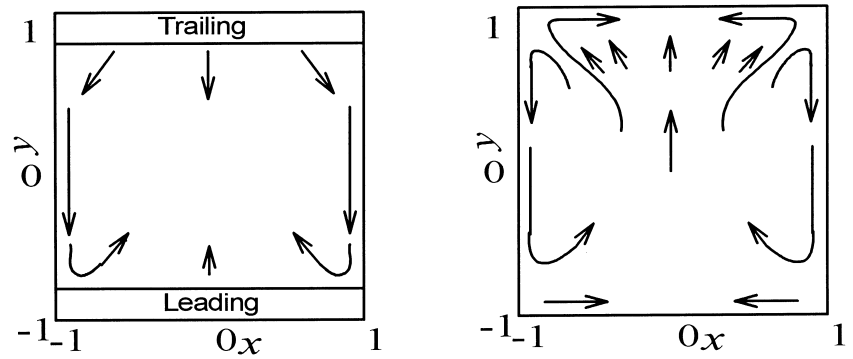

(b)Ro_*=1.0

Fig. 5. Sketch of time-averaged flow pattern in x–y plane drawn from Fig. 4 (aspect ratio, $A_R = 1.0$; left and right figures are at the streamwise locations above rib and between ribs, respectively).

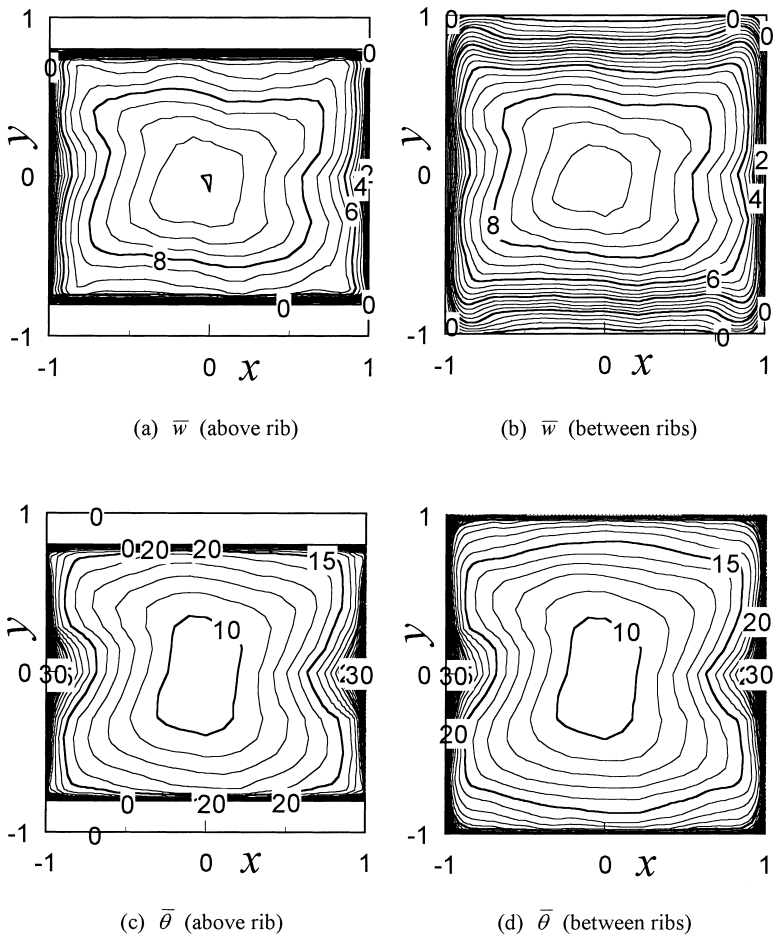

Fig. 6. Isocontours of time-averaged variables in x–y plane for $A_R = 1.0$ and $Ro_* = 0$ (the numbers in each figure show the values for the thick isocontour lines).

mal boundary layer in the mid-plane between the ribs (Fig. 6(b) and (d)). Because this location ($z = 1.1$) is approximately the reattachment point (see Fig. 2(a)), the unsteadiness in the flow separation and reattachment seems to break the similarity between $\bar{w}$ and $\bar{\theta}$, and to make the thermal boundary layer thinner. The secondary flow seen in Fig. 4(a) gives a locally thicker boundary layer on the smooth side walls at $y = 0$ in both velocity and temperature fields.

For the rotating case of Fig. 7, the dissimilarity between the streamwise velocity and temperature fields is observed even in the plane above the rib (Fig. 7(a) and (c)). In the temperature profile (Fig. 7(c) and (d)) the peak shifts to the trailing surface (the upper wall in the figure), and, on the contrary, the peak of the streamwise velocity profile (Fig. 7(a) and (b)) stays at the center or tends to shift to the leading surface (the lower wall in the figure). This dissimilarity was also seen in the turbulent flow of a rotating smooth rectangular duct for transversely flat aspect ratio cases ($A_R = 0.5$ and 0.25) [19]. The shift of the streamwise velocity peak to the suction surface was observed in the turbulent flow of a rotating two-dimensional channel [11], and this shift of the velocity peak was explained by the shift of the zero shear stress location to the suction side because of the direct influence of the Coriolis force on the velocity fluctuating components. The direct influence of the Coriolis force can be understood by considering additional production terms introduced by the rotation in the transport equations of the Reynolds stress; especially, source and sink terms for the wall normal component of the Reynolds normal stress near the pressure and suction surfaces, respectively [11]. The different contribution of the Coriolis force on the turbulent scalar flux may have caused the dissimilarity. The transverse ribs seems to make the flow field two-dimensional by contracting the flow as compared to the smooth duct case, and

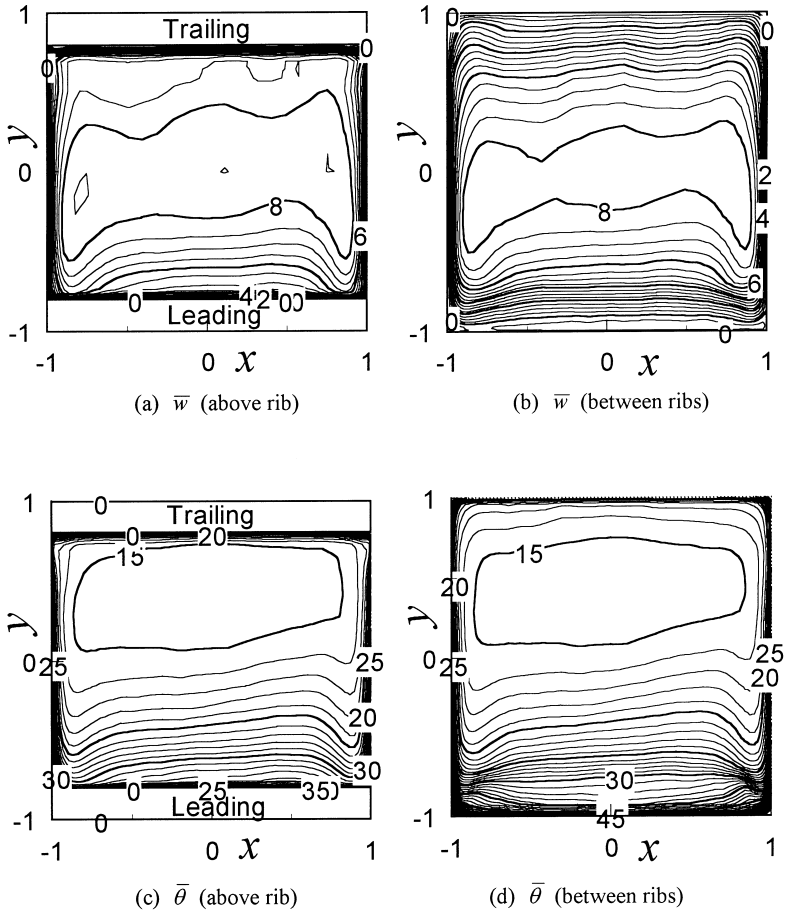

Fig. 7. Isocontours of time-averaged variables in x–y plane for $A_R = 1.0$ and $Ro_* = 1.0$ (the numbers in each figure show the values for the thick isocontour lines).

this may be the reason why the dissimilarity observed in the transversely flat rotating duct was also observed in the present rib-roughened square duct. However, the detailed mechanism of this dissimilarity is not identified yet.

Fig. 8 shows the wall shear stress (Fig. 8(a) and (c)) and the local Nusselt number (Fig. 8(b) and (d)) on the four walls for the stationary case. Both instantaneous (Fig. 8(a) and (b)) and time-averaged (Fig. 8(c) and (d)) values are shown. For the rib area, the value at the rib top surface is shown. The Nusselt number is normalized using the following empirical correlation for a fully developed pipe flow [30]:

$$Nu_\infty = 0.022 Re_m^{0.8} Pr^{0.5}. \quad (7)$$

In the figures, out-of-range values are shown by white and black solid areas for very low and very high values, respectively. In Fig. 8(c), zero shear stress areas are also indicated by solid white. When the instantaneous values are compared in Fig. 8(a) and (b), the locations where the absolute value of wall shear stress becomes large and small are highly correlated to the locations of high and low local Nusselt numbers, respectively. The spots of large positive shear stress indicated by ellipses in Fig. 8(a) are considered to correspond to the sweep motion which transports cooler fluid from the main stream to the wall with high streamwise momentum. Therefore, the high heat transfer at the corresponding spots in Fig. 8(b) is reasonable. On the other hand, the spots of large negative shear stress indicated by circles in Fig. 8(a) are seen in front of the rib, and the spots also correspond to the high heat transfer in Fig. 8(b). This locally large negative shear stress is caused by fluid which impinges on the wall in front of the rib after another impingement on the rib front surface. In front of the rib, a very high heat transfer area is observed in the time-averaged Nusselt number of Fig. 8(d), and this agrees with previous experimental results [7–9]. In the time-averaged shear stress of Fig. 8(c), only a flow separation bubble in front of the rib seems to exist (see Fig.

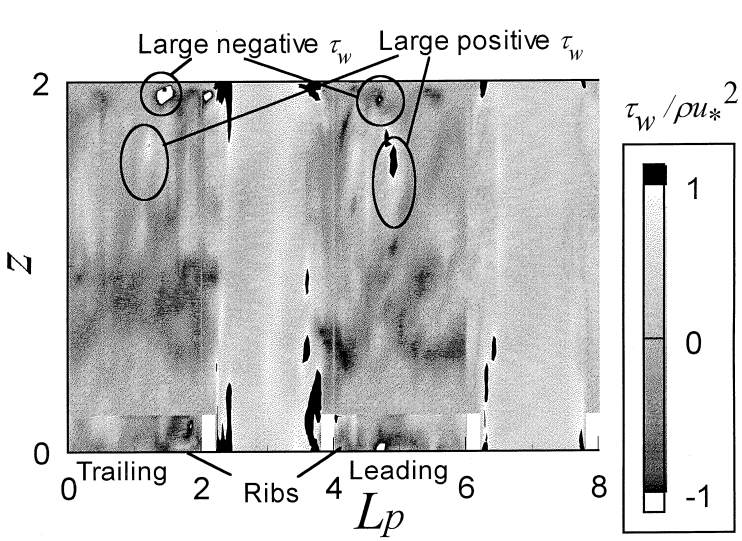

(a) instantaneous wall shear stress

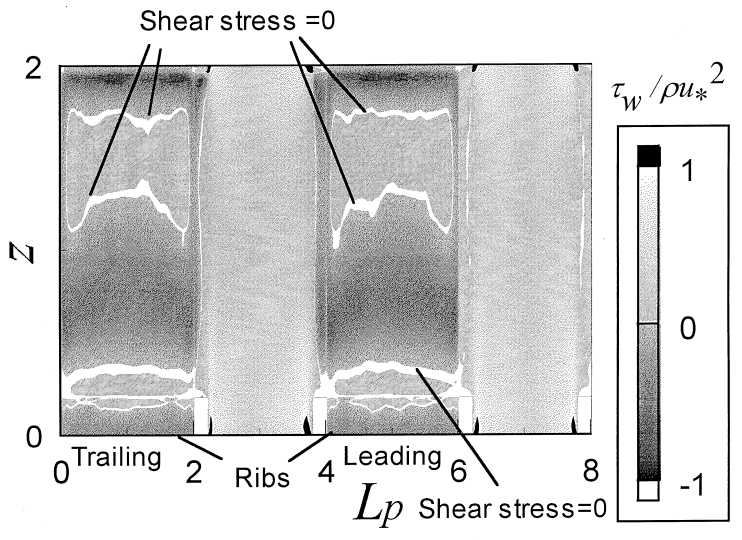

(c) time-averaged wall shear stress

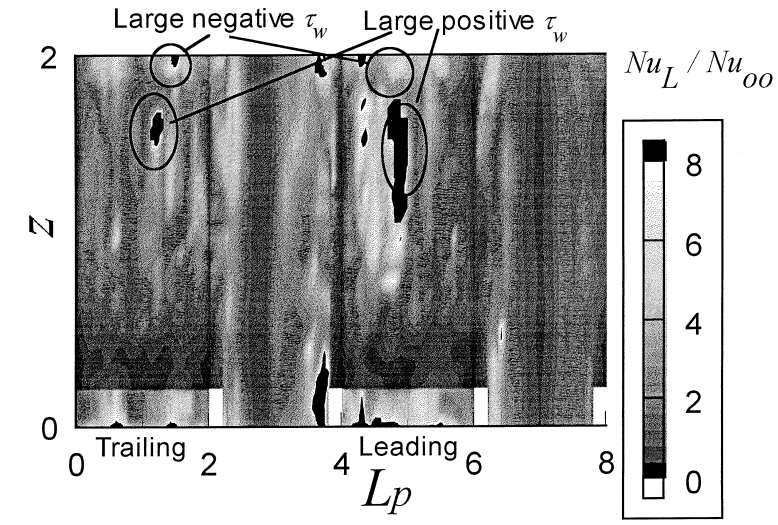

(b) instantaneous Nusselt number

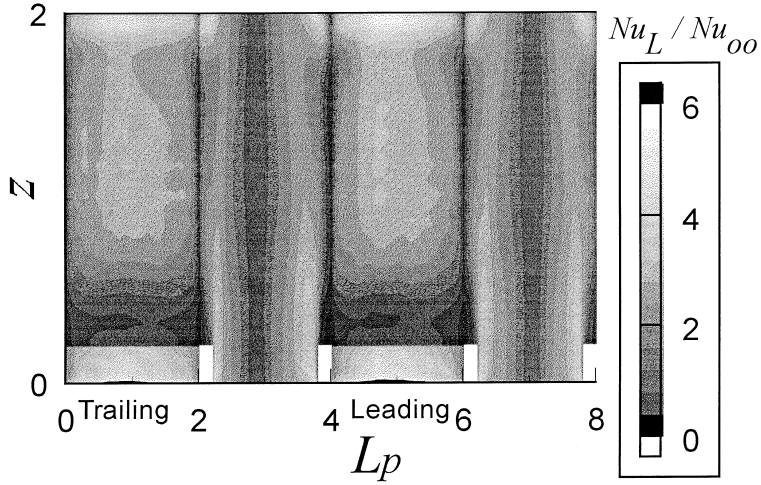

(d) time-averaged Nusselt number

Fig. 8. Spatial variation of wall shear stress and Nusselt number on four walls for $A_R = 1.0$ and $Ro_* = 0$.

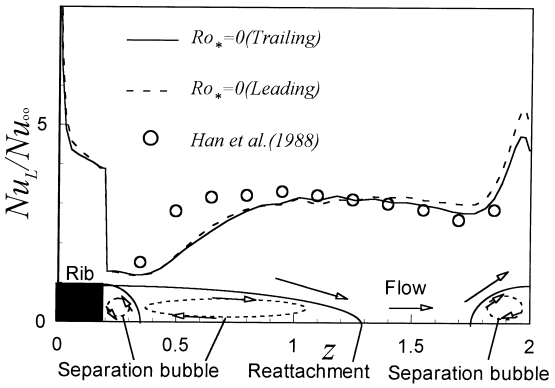

Fig. 9. Local Nusselt number profile at the transverse center ($x = 0$) on rib-roughened walls; experimental data of Han et al. [6] were measured by using the naphthalene sublimation method for $Re_m = 30{,}000$, rib pitch-to-height ratio: 10, and rib height-to-hydraulic diameter ratio: 0.094. The measurement location is around $10D$ downstream from the entrance.

3(a)). In laminar flow, the flow separation in front of the rib stays steady, and the heat transfer becomes very low. On the other hand, the turbulent flow with high streamwise momentum and low temperature impinges on the rib front surface and forms a localized separation cell. Because this cell temporally changes its transverse location and intensity, the heat transfer there becomes high.

Behind the rib, judging from two lines of shear stress being zero there in the time-averaged shear stress variation of Fig. 8(c) and also from the flow pattern in Fig. 2(a) (right) and Fig. 3(a), two separation bubbles rotating in opposite directions to each other exist. In addition to those, there is another separation bubble in front of the rib as mentioned above. In Fig. 8(d), the time-averaged Nusselt number becomes very high on the rib top surface. The heat transfer behind the rib for a time becomes lower because of the flow separation and then takes a first local maximum around the reattachment point. The second local maximum is just in front of the rib. This profile is depicted in Fig. 9 as a streamwise variation of the Nusselt number at the transverse center ($x = 0$). In the figure, the experimental results of Han et al. [6] measured by using the naphthalene sublimation technique are plotted for comparison; their experimental condition is for higher Reynolds number and almost same rib configuration as compared to the present study: $Re_m = 30{,}000$, rib pitch-to-height ratio: 10, and rib height-to-hydraulic diameter ratio: 0.094. In the lower part of the figure, the flow structure schematic is sketched. The numerical results on the trailing and leading walls agree well with each other, and this verifies that the symmetric condition is attained in the statistically averaged value. The agreement between the numerical and experimental results is good, although the experimental results have the peak at the upstream location as compared to the numerical results. The numerical results show the very high peak in front of the rib; the experimental results show a slight increase in front of the rib, although the region very close to the rib is not resolved. In the numerical results, the peak in front of the rib is higher than the peak around the reattachment point which gives the broadened peak. Judging from the comparison between the different spatial variation between the instantaneous and time-averaged fields in Fig. 8, it can be deduced that the reattachment point moves temporally, and therefore the heat transfer enhancement occurs at various locations; this broadens the high heat transfer area around the reattachment point. In this study, the rib side surfaces are adiabatic as explained in the numerical analysis. In order to check the effect of the boundary condition on the appearance of the high heat transfer area in front of the rib, an additional computation was performed by setting the constant heat flux boundary condition on the rib side surfaces; the result verified that the highest peak of the Nusselt number in front of the rib was retained even when the constant heat flux boundary condition was used on the rib side surfaces.

On the smooth side walls, the area around the rib shows very high values in both the wall shear stress and the heat transfer in Fig. 8. This high Nusselt number area was also experimentally observed [8,9], and this high value is formed by the high momentum fluid flowing around the location. On the smooth side walls, the Nusselt number near the central area is lower because of the thicker boundary layer as seen in Fig. 6, although the area around the rib and near the rib-roughened wall gives higher values.

For the rotating case of $Ro_* = 1.0$, the time-averaged values of the wall shear stress and the Nusselt number are shown in Fig. 10. On the trailing wall (pressure surface) of the rotating case (Fig. 10(a)), three separation bubbles are also observed as seen in the stationary case of Fig. 8(c). On the contrary, there are only two separation bubbles on the leading wall (suction surface), and flow reattachment point is not observed as shown in Fig. 2(b) (right) and Fig. 3(b). The separation bubble just behind the rib is weak and cannot be seen in Fig. 10(a). On the smooth side walls in Fig. 10(b), this change in flow structure intensifies and elongates the high heat transfer area around the pressure-side rib in the streamwise direction unlike in the area around the leading-side rib where the high Nusselt number area is not observed. As shown in Fig. 10(b), the Nusselt number on the trailing wall becomes higher than that on the leading wall. On the smooth side wall, the Nusselt number increases from the leading side to the trailing side because of the secondary

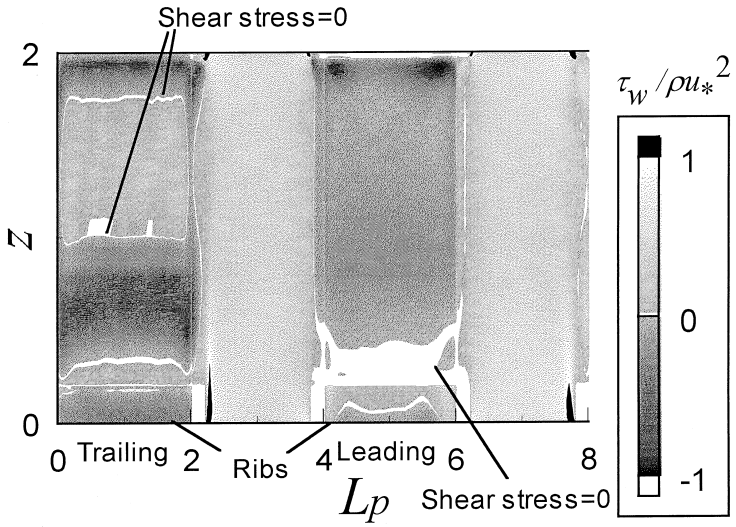

(a) wall shear stress

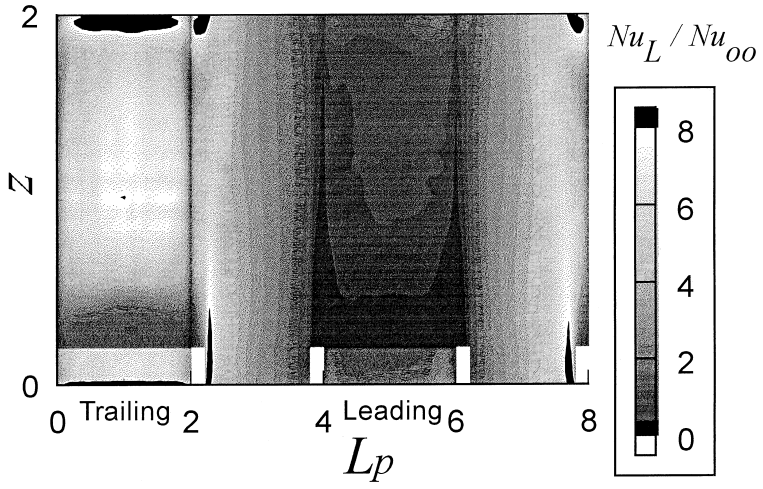

(b) Nusselt number

Fig. 10. Spatial variation of time-averaged wall shear stress and Nusselt number on four walls for $A_R = 1.0$ and $Ro_* = 1.0$.

flow induced by the Coriolis force (see Figs. 4(b) and 5(b)).

3.2. Effect of cross-sectional aspect ratio

Fig. 11 shows the time-averaged velocity vectors in the x–y plane. The aspect ratio is $A_R = 2.0$ for Fig. 11(a) and (b), and $A_R = 4.0$ for Fig. 11(c) and (d). Fig. 11(a) and (c) are for the stationary case, and Fig. 11(b) and (d) are for the rotating case of $Ro_* = 1.0$. The streamwise location of the plane is the same as that in Fig. 4. The general flow structure of the stationary case (Fig. 11(a) and (c)) is similar to that of a square duct (Fig. 4(a)). In the rotating case of Fig. 11(b) and (d), the flow structure is qualitatively similar to the rotating square duct case. That is, the effects of the Coriolis force are seen in the intensified flow near the trailing wall (the upper wall in the figure) and in the dominating Coriolis induced secondary flow near the leading wall (the lower wall in the figure).

In Figs. 12 and 13, the time-averaged variation of the wall shear stress and the Nusselt number is shown for the aspect ratio of $A_R = 2.0$ and 4.0, respectively, for the rotating condition of $Ro_* = 1.0$. Here again, the similar variation to that of the square duct (see Fig. 8) is seen. Those are the disappearance of the flow

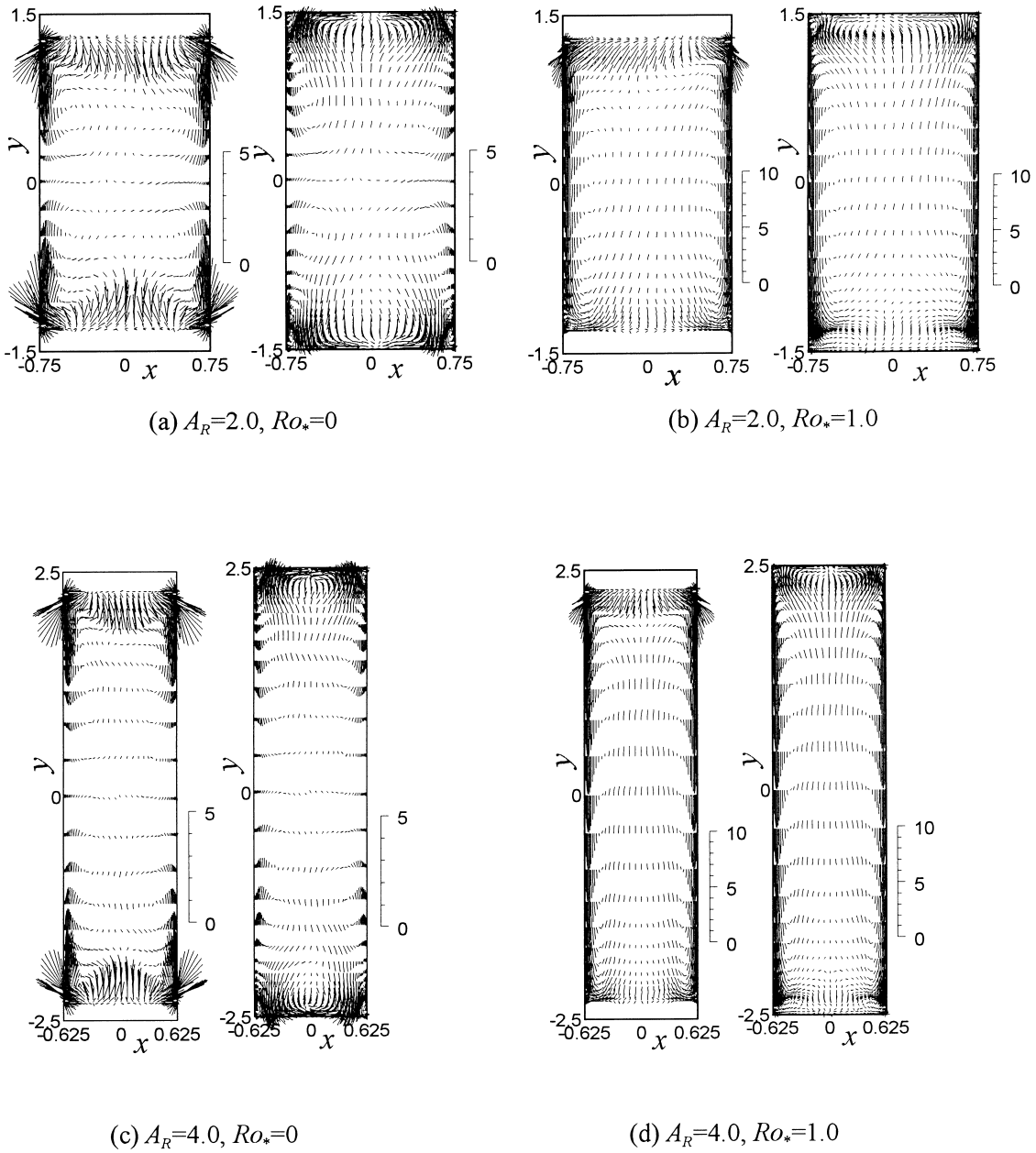

Fig. 11. Time-averaged velocity vectors in x–y plane. (Left and right figures are at the streamwise locations above rib and between ribs, respectively. The scale on the right-hand side of each figure indicates the vector magnitude.)

reattachment point on the leading wall, increased and decreased Nusselt numbers on the trailing and leading walls, respectively, and high Nusselt number area on the smooth side wall around the pressure-side rib.

3.3. Comparison in wall-averaged and duct-averaged values

Fig. 14 shows the dependency of the friction coefficient, C_f, and the wall-averaged Nusselt number, Nu_w, on the rotation number, Ro_m. The friction coefficient was calculated by using the mean streamwise pressure gradient given as 2 in the computation (see Eq. (1)), because the pressure loss in a rib-roughened duct consists of skin friction and form drag which results from the pressure difference between the rib front and rear surfaces [8]. The Nusselt number and the friction coefficient are normalized by using Nu_∞ in

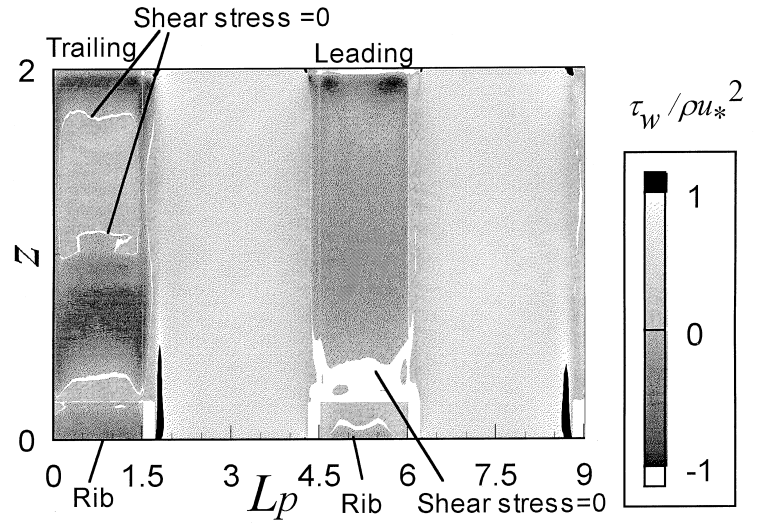

(a) wall shear stress

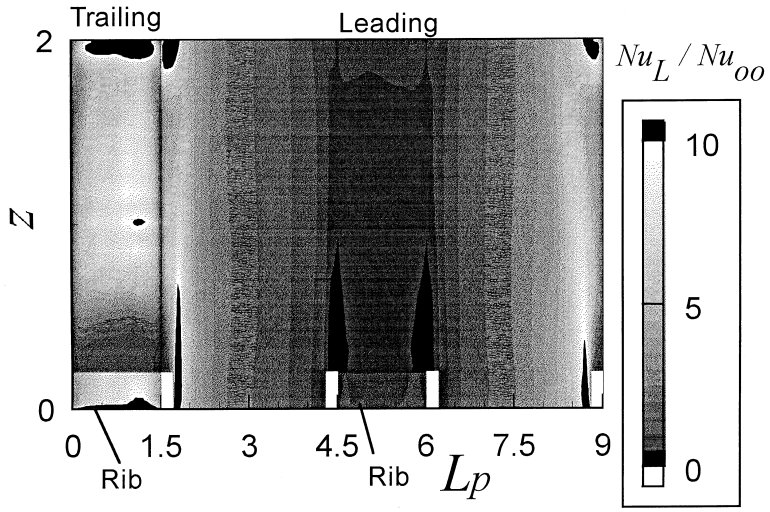

(b) Nusselt number

Fig. 12. Spatial variation of time-averaged wall shear stress and Nusselt number on four walls for $A_R = 2.0$ and $Ro_* = 1.0$.

Eq. (7) and C_{fB} in the following Blasius equation:

$$C_{fB} = 0.079 Re_m^{-0.25}. \quad (8)$$

In this figure, the rotation number is based on the mean velocity and the hydraulic diameter. Because it is widely used in correlating experimental results, this definition was used to make a reference by other researchers easier. In the figure, symbols are the present results of 400,000 time steps with the second order finite difference, and lines are those of reduced sample size by the factor of one-tenth (40,000 time steps) with the fourth order finite difference for $A_R = 1.0$ [20] and with the second order finite difference for $A_R = 2.0$ and 4.0. The results with large sample size agree well with those of smaller sample size. This implies that the wall-averaged (or duct-averaged) values are reliable due to the average on a certain area even when a statistically symmetric condition in a local value is not attained completely. In the case of $A_R = 1.0$, Nu_w on the trailing wall (pressure surface) shows a monotonic increase as the rotation number increases. On the other hand, that on the leading wall (suction surface) decreases monotonically. On the smooth side walls, Nu_w shows a slight increase. In most of the previous experimental studies, the Nusselt number on the smooth side wall was measured with transversely low resolution (mostly, only one measure-

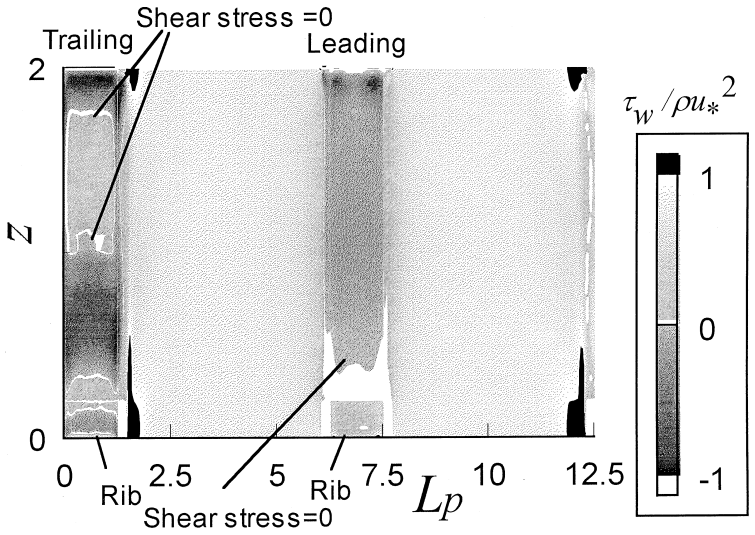

(a) wall shear stress

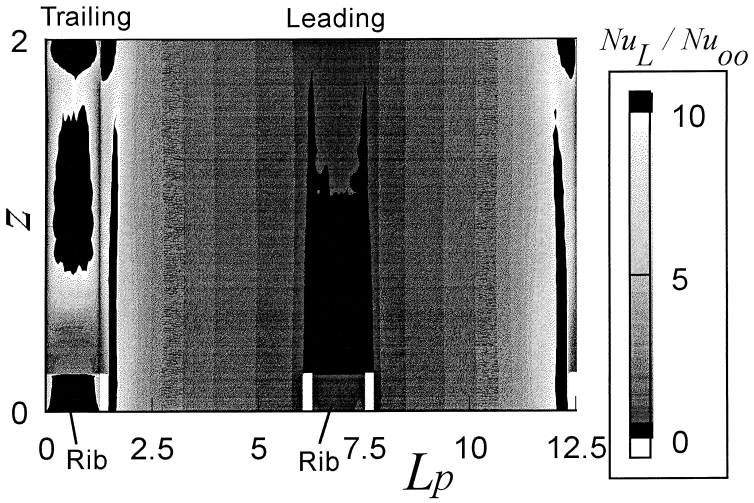

(b) Nusselt number

Fig. 13. Spatial variation of time-averaged wall shear stress and Nusselt number on four walls for $A_R = 4.0$ and $Ro_* = 1.0$.

ment point at the transverse center), and from the data the Nusselt number on the smooth side wall was correlated, for example, to be larger by 25% than the fully developed value of Nu_∞ [31]. However, as seen in Fig. 8, the Nusselt number on the smooth side wall is high especially around the rib, and the wall-averaged value shows a comparable value to that on the rib-roughened wall: for $Ro_* = 0$ in Fig. 14, the Nusselt number ratio, Nu_w/Nu_∞, is 2.0 on the smooth side wall and 2.2 on the rib-roughened wall. When the aspect ratio becomes larger, the difference in the heat transfer on the trailing and leading walls becomes larger. This seems to be caused by the intensified Coriolis induced secondary flow because of the larger velocity variation in the transverse direction in the case of larger aspect ratio (transversely narrow shape) [19].

Fig. 15 shows the duct-averaged result of the friction coefficient, C_f, and the Colburn's j factor. In the stationary case which is displayed by the right most plot of each symbol, the result of $A_R = 4.0$ becomes the smallest because of its lowest fraction of rib-roughened area among the aspect ratios examined. However, as explained above, the effect of rotation is the most significant for $A_R = 4.0$. Consequently, the increase

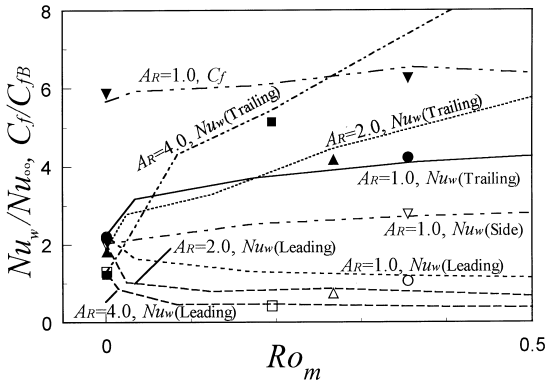

Fig. 14. Effect of rotation on friction coefficient, C_f, and wall-averaged Nusselt number, Nu_w (symbols are for aspect ratio, A_R, •○: 1.0, ▲△: 2.0, ■□: 4.0; filled and open symbols are for trailing and leading walls, respectively, except the following symbols, ▽ : Nu_w on side wall for $A_R = 1.0$, ▼ : C_f for $A_R = 1.0$. Lines are for 1/10 sample size results (40,000 time steps)).

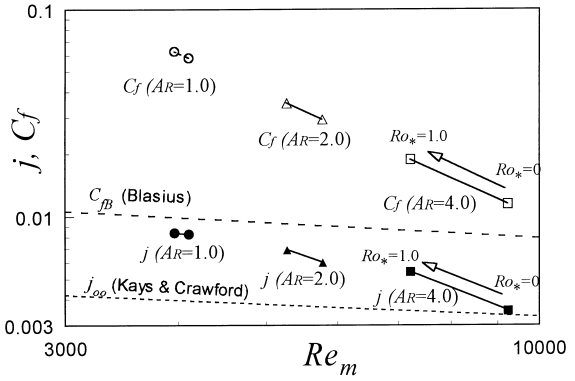

Fig. 15. Effect of rotation and cross-sectional aspect ratio on friction coefficient, C_f, and Colburn's j factor (for each symbol right and left plots are for $Ro_* = 0$ and 1.0, respectively).

rate caused by the rotation is the largest for $A_R = 4.0$. These situations are summarized in Table 1. In the stationary case of $A_R = 1.0$, C_f is about six times as large as the empirical value of the Blasius equation, C_{fB}, and the Colburn's j factor is about twice as large as the empirical value of Kays and Crawford [30], Nu_∞ (or j_∞). This result is within the scatter of the previous experimental results [8]. The effect of rotation is more strongly seen in C_f as compared to j as seen in Table 1.

4. Conclusions

The correlation between the absolute value of the wall shear stress and the heat transfer was high. Especially in front of the rib, large negative value of the wall shear stress was highly correlated to the high heat transfer in the instantaneous field. This led to a very high value of the time-averaged heat transfer in front of the rib. On the smooth side wall, the heat transfer became very high around the rib, and the wall-averaged value on the smooth side wall became comparable to that on the rib-roughened wall. The effect of rotation appeared in the larger spatial variation of the heat transfer on four walls; that is, the increased and decreased heat transfer on the pressure and suction sides, respectively.

In the rotating case, the dissimilarity between the velocity and temperature fields was seen in the shift of the profile peak to the opposite directions. The dissimilarity may be induced by the two-dimensionality caused by the transverse rib installation and the different contribution of the Coriolis force on the fluctuating velocity and temperature fields. In the stationary case, the result of the higher aspect ratio ducts ($A_R = 2.0$ and 4.0) showed the smaller increase in both the friction coefficient, C_f, and the Colburn's j factor because of their smaller fraction of the rib-roughened area as compared to the square duct. However, the higher aspect ratio ducts were more strongly affected by the Coriolis force, and the increase by the rotation was larger for larger aspect ratio among the three cases investigated ($A_R = 1.0$, 2.0, and 4.0).

Table 1
Increase factors in friction coefficient, C_f, and Colburn's j factor caused by rotation and aspect ratio

	$A_R = 1.0$		$A_R = 2.0$		$A_R = 4.0$	
	C_f/C_{fB}	j/j_∞	C_f/C_{fB}	j/j_∞	C_f/C_{fB}	j/j_∞
$Ro_* = 0$	5.89	2.09	3.25	1.65	1.43	1.06
$Ro_* = 1.0$	6.28	2.11	3.81	1.85	2.20	1.54
Increase by rotation (%)	7	1	17	12	54	45

References

[1] B. Lakshminarayana, Fluid Dynamics and Heat Transfer of Turbomachinery, Wiley, New York, 1996, pp. 597–721 (Chapter 7).

[2] S.V. Ekkad, J.C. Han, Detailed heat transfer distributions in two-pass square channels with rib turbulators, Int. J. Heat Mass Transf 40-11 (1997) 2525–2537.

[3] S. Mochizuki, A. Murata, M. Fukunaga, Effects of rib arrangements on pressure drop and heat transfer in a rib-roughened channel with a sharp 180 turn, Trans. ASME, J. of Turbomachinery 119 (1997) 610–616.

[4] S. Mochizuki, M. Beier, A. Murata, T. Okamura, Y. Hashidate, Detailed measurement of convective heat transfer in rotating two-pass rib-roughened coolant channels, ASME Paper, 96-TA-6, 1996.

[5] A. Murata, S. Mochizuki, T. Takahashi, Local heat transfer measurements of an orthogonally rotating square duct with angled rib turbulators, Int. J. Heat Mass Transf 42 (1999) 3047–3056.

[6] J.C. Han, P.R. Chandra, S.C. Lau, Local heat/mass transfer distribution around sharp 180 deg turns in two-pass smooth and rib-roughened channels, Trans. ASME, J. of Heat Transf 110 (1988) 91–98.

[7] M. Hirota, H. Fujita, H. Yokosawa, T. Nakayama, T. Tanaka, Heat (mass) transfer characteristics in the entrance region of rib-roughened rectangular ducts, Trans. JSME(B) (in Japanese) 63-603 (1997) 1327–1335.

[8] G. Rau, M. Cakan, D. Moeller, T. Arts, The effect of periodic ribs on the local aerodynamic and heat transfer performance of a straight cooling channel, ASME Paper, 96-GT-541, 1996.

[9] J.W. Baughn, X. Yan, Local heat transfer measurements in square ducts with transverse ribs, Enhanced Heat Transfer ASME HTD-202 (1992) 1–7.

[10] T. Bo, H. Iacovides, B.E. Launder, Developing buoyancy-modified turbulent flow in ducts rotating in orthogonal mode, Trans. ASME, J. of Turbomachinery 117 (1995) 474–484.

[11] B.E. Launder, D.P. Tselepidakis, B.A. Younis, A second-moment closure study of rotating channel flow, J. Fluid Mech 183 (1987) 63–75.

[12] A. Huser, S. Biringen, Direct numerical simulation of turbulent flow in a square duct, J. Fluid Mech 257 (1993) 65–95.

[13] S. Gavrilakis, Numerical simulation of low Reynolds number turbulent flow through a straight square duct, J. Fluid Mech 244 (1992) 101–129.

[14] R.K. Madabhushi, S.P. Vanka, Large eddy simulation of turbulence-driven secondary flow in a square duct, Phys. Fluids A3-11 (1991) 2734–2745.

[15] T. Kajishima, Y. Miyake, T. Nishimoto, Large eddy simulation of turbulent flow in a square duct, Trans. JSME (in Japanese) 57-540 (1991) 2530–2537.

[16] C. Prakash, R. Zerkle, Prediction of turbulent flow and heat transfer in a ribbed rectangular duct with and without rotation, Trans. ASME, J. of Turbomachinery 117 (1995) 255–264.

[17] Analysis of Turbulent Flows, Computational fluid dynamics series 3 (in Japanese), in: H. Miyata (Ed.), University of Tokyo Press, Tokyo, 1995, pp. 79, 97.

[18] A. Murata, S. Mochizuki, Large eddy simulation of turbulent heat transfer in an orthogonally rotating square duct, Trans. JSME(B) (in Japanese) 64-623 (1998) 2196–2201.

[19] A. Murata, S. Mochizuki, Effect of cross-sectional aspect ratio on turbulent heat transfer in an orthogonally rotating rectangular smooth duct, Int. J. Heat Mass Transf 42 (1999) 3803–3814.

[20] A. Murata, S. Mochizuki, Large eddy simulation applied to internal forced-convection cooling of gas-turbine blades, in: Heat Transfer 1998, Proceedings of Eleventh International Heat Transf. Conf., vol. 6, Taylor and Francis, London, 1998, pp. 565–570.

[21] M.E. Taslim, S.D. Spring, Effect of turbulator profile and spacing on heat transfer and friction in a channel, J. of Thermophys. and Heat Transf 8-3 (1994) 555–562.

[22] G.J. Korotky, M.E. Taslim, Rib heat transfer coefficient measurements in a rib-roughened square passage, ASME Paper, 96-GT-356, 1996.

[23] S.V. Patankar, C.H. Liu, E.M. Sparrow, Fully developed flow and heat transfer in ducts having streamwise-periodic variations of cross-sectional area, Trans. ASME, J. of Heat Transf 99 (1977) 180–186.

[24] M. Germano, U. Piomelli, P. Moin, W.H. Cabot, A dynamic subgrid-scale eddy viscosity model, Phys. Fluids A3-7 (1991) 1760–1765.

[25] D.K. Lilly, A proposed modification of the Germano subgrid-scale closure method, Phys. Fluids A4-3 (1992) 633–635.

[26] P. Moin, K. Squires, W. Cabot, S. Lee, A dynamic subgrid-scale model for compressible turbulence and scalar transport, Phys. Fluids A3-11 (1991) 2746–2757.

[27] Y. Morinishi, Conservative properties of finite difference schemes for incompressible flow (second report, schemes in staggered and collocated grid systems), Trans. JSME(B) (in Japanese) 62 (1996) 4098–4105.

[28] A.A. Amsden, F.H. Harlow, A simplified MAC technique for incompressible fluid flow calculations, J. of Comp. Phys 6 (1970) 322–325.

[29] H. Yokosawa, H. Fujita, M. Hirota, S. Iwata, Measurement of turbulent flow in a square duct with roughened walls on two opposite sides, Int. J. Heat and Fluid Flow 10-2 (1989) 125–130.

[30] W.M. Kays, M.E. Crawford, Convective Heat and Mass Transfer, 3rd ed., McGraw-Hill, New York, 1993, p. 316.

[31] J.C. Han, Heat transfer and friction in channels with two opposite rib-roughened walls, Trans. ASME, J. of Heat Transf 106 (1984) 774–781.